

Search for Neutrinoless Double-Beta Decay of ^{76}Ge with a Natural Broad Energy Germanium Detector

W. H. Dai,¹ H. Ma,^{1,*} Q. Yue,^{1,†} Z. She,¹ K. J. Kang,¹ Y. J. Li,¹ M. Agartioglu,^{2,‡} H. P. An,^{1,3} J. P. Chang,⁴ Y. H. Chen,⁵ J. P. Cheng,^{1,6} Z. Deng,¹ C. H. Fang,⁷ H. Gong,¹ Q. J. Guo,⁸ X. P. Geng,¹ X. Y. Guo,⁵ L. He,⁴ S. M. He,⁵ J. W. Hu,¹ H. X. Huang,⁹ T. C. Huang,¹⁰ H. T. Jia,⁷ X. Jiang,⁷ H. B. Li,^{2,‡} H. Li,⁴ J. M. Li,¹ J. Li,¹ Q. Y. Li,⁷ R. M. J. Li,⁷ X. Li,⁹ X. Q. Li,¹¹ Y. L. Li,¹ B. Liao,⁶ Y. F. Liang,¹ F. K. Lin,^{2,‡} S. T. Lin,⁷ S. K. Liu,⁷ Y. Liu,⁷ Y. D. Liu,⁶ Y. Y. Liu,⁶ Z. Z. Liu,¹ Y. C. Mao,⁸ Q. Y. Nie,¹ J. H. Ning,⁵ H. Pan,⁴ N. C. Qi,⁵ J. Ren,⁹ X. C. Ruan,⁹ K. Saraswat,^{2,‡} M. K. Singh,^{2,12,‡} T. X. Sun,⁶ V. Sharma,^{2,12,‡} C. J. Tang,⁷ W. Y. Tang,¹ Y. Tian,¹ G. F. Wang,⁶ L. Wang,¹³ Q. Wang,^{1,3} Y. Wang,^{1,3} Y. X. Wang,⁸ H. T. Wong,^{2,‡} S. Y. Wu,⁵ Y. C. Wu,¹ R. Xu,¹ H. Y. Xing,⁷ Y. Xu,¹¹ T. Xue,¹ L. T. Yang,¹ Y. L. Yan,⁷ C. H. Yeh,^{2,‡} N. Yi,¹ C. X. Yu,¹¹ H. J. Yu,⁴ J. F. Yue,⁵ M. Zeng,¹ Z. Zeng,¹ B. T. Zhang,¹ F. S. Zhang,⁶ J. F. Zhou,⁵ J. J. Zhu,⁷ K. K. Zhang,⁷ M. G. Zhao,¹¹ Z. Y. Zhang,¹ Z. H. Zhang,¹ and Z. Y. Zhou⁹

(CDEX Collaboration)

¹Key Laboratory of Particle and Radiation Imaging (Ministry of Education)
and Department of Engineering Physics, Tsinghua University, Beijing 100084

²Institute of Physics, Academia Sinica, Taipei 11529

³Department of Physics, Tsinghua University, Beijing 100084

⁴NUCTECH Company, Beijing 100084

⁵YaLong River Hydropower Development Company, Chengdu 610051

⁶College of Nuclear Science and Technology, Beijing Normal University, Beijing 100875

⁷College of Physics, Sichuan University, Chengdu 610065

⁸School of Physics, Peking University, Beijing 100871

⁹Department of Nuclear Physics, China Institute of Atomic Energy, Beijing 102413

¹⁰Sino-French Institute of Nuclear and Technology, Sun Yat-sen University, Zhuhai 519082

¹¹School of Physics, Nankai University, Tianjin 300071

¹²Department of Physics, Banaras Hindu University, Varanasi 221005

¹³Department of Physics, Beijing Normal University, Beijing 100875

(Dated: May 24, 2022)

A natural broad energy germanium (BEGe) detector is operated to search for the neutrinoless double-beta ($0\nu\beta\beta$) decay of ^{76}Ge in the China Jinping Underground Laboratory (CJPL). The setup of the prototype facility, characteristics of the BEGe detector, background reduction methods and data analysis are described in this paper. A background index of 6.4×10^{-3} counts/(keV·kg·day) is achieved and 1.86 times lower than our previous result of the CDEX-1 detector. No signal is observed with an exposure of 186.4 kg·day, thus a limit on the half life of ^{76}Ge $0\nu\beta\beta$ decay is set at $T_{1/2}^{0\nu} > 5.62 \times 10^{22}$ yr at 90% C.L.. The limit corresponds to an effective Majorana neutrino mass in the range of 4.6 ~ 10.3 eV, dependent on the nuclear matrix elements.

Key words: Neutrinoless double-beta decay, BEGe, ^{76}Ge , CJPL.

I. INTRODUCTION

Evidences for non-zero mass neutrinos have been provided by the atmospheric and solar neutrino oscillation experiments [1-4] over the last two decades. Neutrinos can obtain their masses by a Majorana mass term if they are their own anti-particles [5]. The Majorana nature of the neutrinos leads to lepton number violation and naturally emerges in many beyond-the-Standard Model theories [6]. It also emerges in leading theories that explain the dominance of matter over antimatter in the Universe [7,8].

The search for neutrinoless double-beta ($0\nu\beta\beta$) decay is considered the most promising way to prove the Majorana nature of neutrinos [9]. Furthermore, a measurement of the $0\nu\beta\beta$ decay rate, which depends on the effective Majorana mass, can indicate the mass hierarchy and the absolute mass scale of neutrinos.

Assuming the Majorana nature of neutrinos, the neutrinoless double-beta decay, $(A, Z) \rightarrow (A, Z + 2) + 2e^-$, is permitted in $2\nu\beta\beta$ decay isotopes [10]. A number of experiments have conducted $0\nu\beta\beta$ decay search in various candidate isotopes, for instance ^{76}Ge [11-14], ^{136}Xe [15,16], ^{130}Te [17,18], ^{100}Mo [19,20], via different detection technologies, including semiconductor detector [11-13], time projection chamber [15] and cryogenic bolometer [17,21].

High purity germanium (HPGe), serving as both target nuclei and detector, is an ideal medium for detecting $0\nu\beta\beta$ decays because of its high energy resolution, low

* mahao@tsinghua.edu.cn

† yueq@mail.tsinghua.edu.cn

‡ Participating as a member of TEXONO Collaboration

internal background, and high detection efficiency [22]. Several experiments have been searched for neutrinoless double-beta decay in ^{76}Ge via the HPGe technology, such as Gerda [12] and Majorana [13]. Currently, the Gerda experiment, operating enriched germanium detector array in liquid argon to detect $0\nu\beta\beta$ decay of ^{76}Ge , achieves the lowest background level in the $Q_{\beta\beta}$ energy region and gives the most stringent constraint on the ^{76}Ge $0\nu\beta\beta$ half-life [12]. The Gerda and the Majorana collaborations are now merged into the Legend collaboration and are proposing a 200 kg-scale $0\nu\beta\beta$ experiment (Legend-200) aiming at setting the $0\nu\beta\beta$ decay half-life limit of ^{76}Ge at 10^{27} yr [14].

The CDEX collaboration has given its first $0\nu\beta\beta$ limit of $T_{1/2}^{0\nu} > 6.4 \times 10^{22}$ yr for a p-type point contact high-purity germanium detector [23]. A next-generation $0\nu\beta\beta$ experiment CDEX-300 ν has been proposed in CJPL-II [24]. The CDEX-300 ν experiment aims at achieving a discovery potential that reaches the inverted-ordering neutrino mass scale region with 1-ton \cdot yr exposure.

In this work, we set up a prototype facility in CJPL to study characteristics of a BEGe detector and novel background suppression techniques for future applications in the CDEX-300 ν experiment. Data acquisition, analysis and pulse shape discrimination procedures are established and tested. And a $0\nu\beta\beta$ result is given by analyzing a 186.4 kg-day exposure data using an unbinned extended profile likelihood method.

II. EXPERIMENT SETUP

A 1088.5 g natural low background broad energy germanium (BEGe) detector made by CANBERRA is used in our experiment. It is fabricated with a natural p-type germanium crystal with 91.1 mm in diameter and 31.4 mm in height. The atom fraction of ^{76}Ge in the crystal is 7.83%. The BEGe detector operates at 4500 V high voltage. The output from the p+ electrode is fed into a Canberra 2002C RC preamplifier to cover a wide dynamic energy range of up to 3.5 MeV for the $0\nu\beta\beta$ decay search experiment. The preamplifier output is digitized by a flash analog-to-digital convertor (FADC) at a 500 MHz sampling rate and recorded by the CAEN Scope software. The trigger threshold of FADC is set to only record events with energy above 500 keV, and the trigger rate is approximately 0.005 cps during data taking. A schematic diagram of the data acquisition (DAQ) system is shown in Fig. 1.

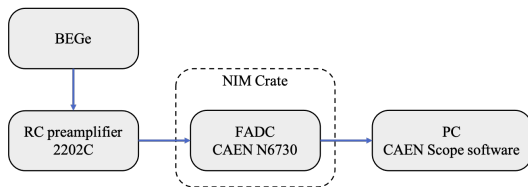


FIG. 1. Schematic diagram of the DAQ system.

An experiment setup is built in the polyethylene (PE) room of the CJPL-I experiment hall. The over 2400 m rock overburden provides natural shields against the cosmic rays, and the cosmic muon flux in CJPL is about $(2.0 \pm 0.4) \times 10^{-10} \text{ cm}^{-2}\text{s}^{-1}$ [25]. Environmental neutrons are shielded by the 1m thick wall of the PE room, the thermal neutron flux inside the PE room is measured to be $(3.18 \pm 0.97) \times 10^{-8} \text{ cm}^{-2}\text{s}^{-1}$ [26].

A passive shielding structure is built to shield the ambient radioactivity. As shown in Fig. 2, the detector crystal is shielded with a 20 cm lead, a 20 cm borated polyethylene, and a minimum of 20 cm copper from outside to inside. The outmost 20 cm lead is used to shield the ambient gamma rays. The middle 20 cm borated polyethylene acts as a thermal neutron absorber. The innermost copper shield is made of low background oxygen-free high conductivity (OFHC) copper to shield the residual gamma rays surviving the outer shields. The space within the copper shields is continuously flushed with high purity nitrogen gas from a pressurized Dewar to exclude the radon.

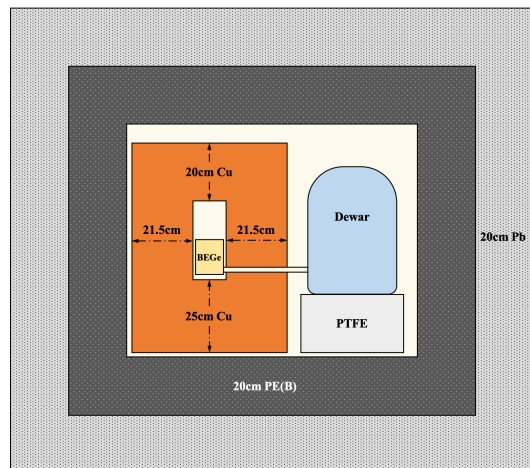


FIG. 2. Schematic diagram of the experimental set up; The setup is located in a PE room (not shown) with 1 m thick PE wall.

III. DATA ANALYSIS

A. Events selection and energy calibration

The baseline level of the 500 MHz FADC is used to monitor the working condition of the detector, as shown in Fig. 3. Data taking starts on 2020/06/01 and ends on 2021/01/10. The gap from 2020/10/08 to 2020/11/02 was due to the unstable power supply caused by the construction of CJPL-II. Periods with unstable baseline levels are excluded from analysis (shadow regions in Fig. 3). On December 15, 2020, an accidental power failure causes a significant shift in the baseline level.

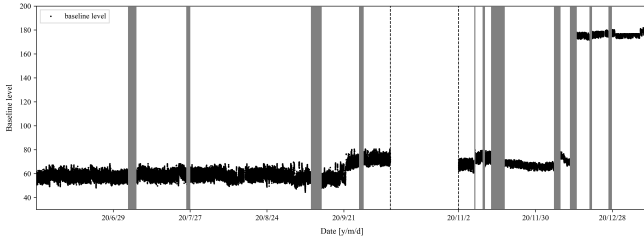


FIG. 3. Baseline level of the detector during data taking. The shadow regions are excluded from analysis because of their unstable baseline level. A major shift of baseline level on 2020/12/05 is caused by an accidental power failure.

After excluding the shadow region in Fig. 3, the remaining 186.4 kg-day exposure data is divided into 9 datasets depending on the time and the baseline level of the detector. Data selections and the energy calibration are performed independently in each dataset.

The recorded events are selected by a noise cut and a data quality cut to remove noise events and events with abnormal baseline levels. Unphysical events, most bursts of noise, are rejected by the noise cut: events with minimum pulse values much lower than their baseline levels (10% of trigger threshold) are rejected. Events with baseline level not in ± 3 times standard deviation of the average baseline level are rejected by the data quality cut. Fig. 4 shows baseline levels and the acceptance region of the data quality cut for one dataset.

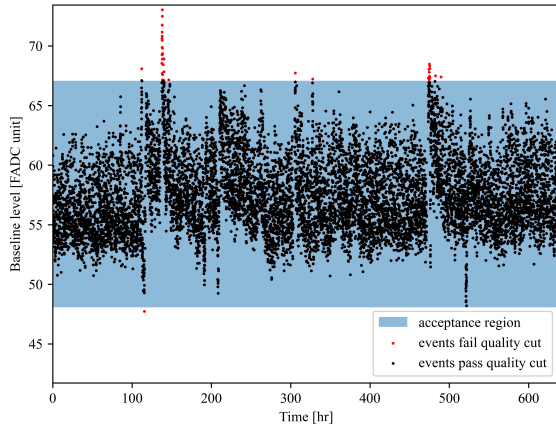


FIG. 4. Baseline levels and the data quality cut of one dataset, red points are events that fail the data quality cuts, the acceptance region is labeled in blue.

Amplitudes are extracted from the remaining charge pulses via a trapezoidal filter [27,28]. The filter parameters, rise time and flat time, are set as $8 \mu\text{s}$ and $1 \mu\text{s}$, respectively. As shown in Fig. 5, the trapezoidal filter converges the raw charge pulse to a trapezoid pulse in which the height of the trapezoid indicates the ampli-

tude of the raw pulse.

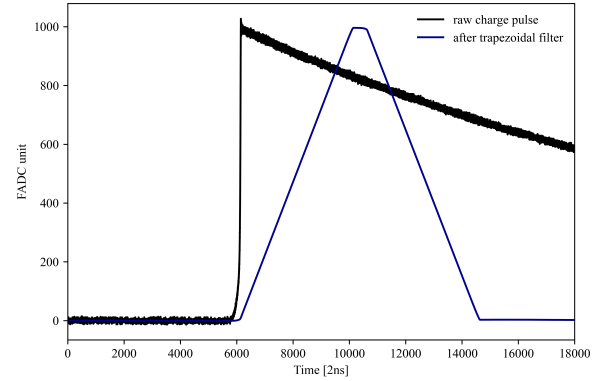


FIG. 5. An example of a charge pulse before/after the trapezoidal filter, the baseline of the charge pulse has been subtracted.

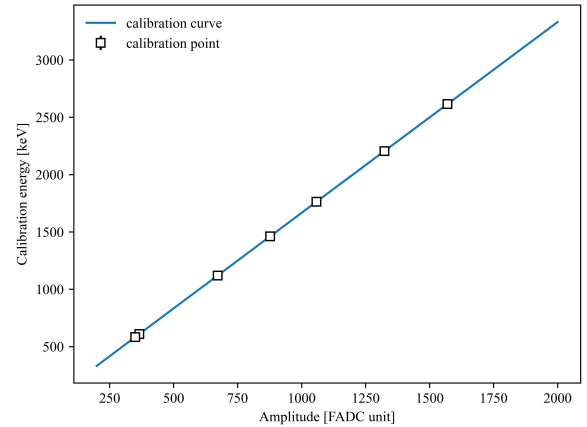


FIG. 6. The energy calibration of one of 11 datasets.

Energy calibrations are performed in each dataset using characteristic gamma peaks from natural radionuclides in the detector and its surrounding materials. Seven peaks from ^{208}Tl (583.3 keV, 2614.5 keV), ^{214}Bi (609.3 keV, 1120.3 keV, 1764.5 keV, 2204.1 keV), and ^{40}K (1460.8 keV) are used in calibrations. Each peak is fitted with a Gaussian function coupled with a linear background to determine the peak position. A second-order polynomial is used to convert amplitude to energy. Fig. 6 shows the calibration curve of one dataset. After combining calibrations of all datasets, a maximum 1.5 keV residual is found in the calibration curve. A quadratic correction [29] is applied in the combined data to reduce the residuals of fitted energy, as shown in Fig. 7. After quadratic correction, the maximum residual is below 0.7 keV for all seven characteristic gamma peaks.

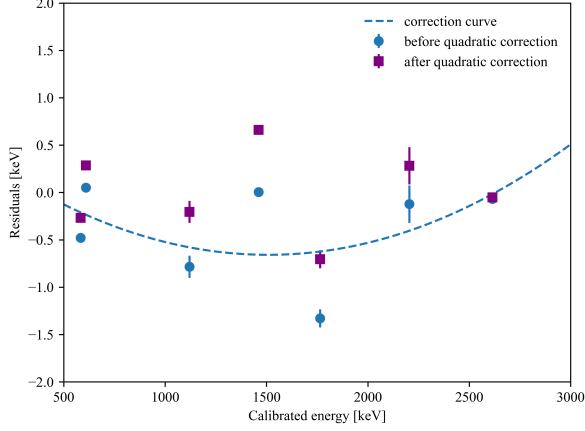


FIG. 7. Quadratic correction of the combined data, the residuals of the calibrated energy are fitted with a quadratic function.

B. Pulse shape discrimination

Since the ranges in a germanium crystal of the two electrons of a $0\nu\beta\beta$ decay event are of the order of 1 mm, $0\nu\beta\beta$ events are typical single-site events (SSEs). High energy gamma rays are expected to deposit their energies at multiple sites featuring the so-called multi-site events (MSEs).

A pulse shape discrimination (PSD) method can be used to discriminate between single-site events and multi-site events in a BEGe detector [30,31]. The PSD method relies on the A/E parameter, in which A is the maximum amplitude of the current pulse and E is the reconstructed energy. The current pulse is extracted from the charge pulse by a moving average differential filter. Fig. 8 shows charge and current pulses of a typical SSE and MSE, respectively. SSEs deposit energies in a small range of area. The current of a SSE has one peak, with an amplitude A proportional to the energy E. MSEs deposit energies in multiple detector positions, leading to multi-peaks in current pulses and lower A/E values than those of SSEs.

A ^{228}Th calibration experiment is conducted to determine the acceptance region of the A/E cut, the detector is irradiated by a ^{228}Th source to create double escape events from ^{208}Tl 2614.5 keV γ -rays. Events in the 1592.5 keV double escape peak (DEP) have a similar profile as the $0\nu\beta\beta$ events [30] and therefore are used as proxies of SSEs. Events in the single escape peak (SEP) are typical two-site events and are used as proxies of MSEs. The A/E distribution of DEP events is fitted with a Gaussian function to determine the mean ($\mu_{A/E}^{SSE}$) and standard deviation ($\sigma_{A/E}^{SSE}$) of A/E parameters for SSEs. The acceptance region of the A/E cut is set to $(\mu_{A/E}^{SSE} \pm 5\sigma_{A/E}^{SSE})$ and leads to a 93% survival rate of the DEP events, and a 5% survival rate of the SEP events.

Fig. 9 shows A/E discriminations applied in the ^{228}Th

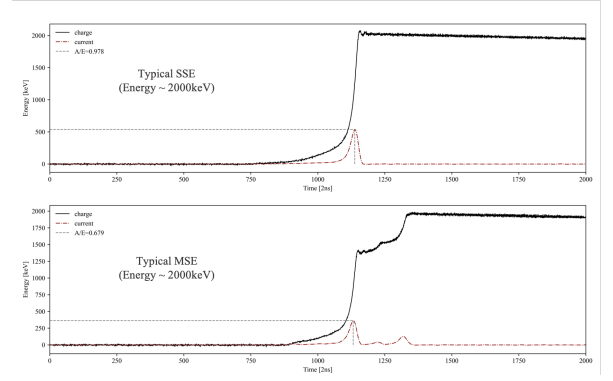


FIG. 8. Typical charge and current pulses of a SSE / MSE, the current pulses have been rescaled for demonstration.

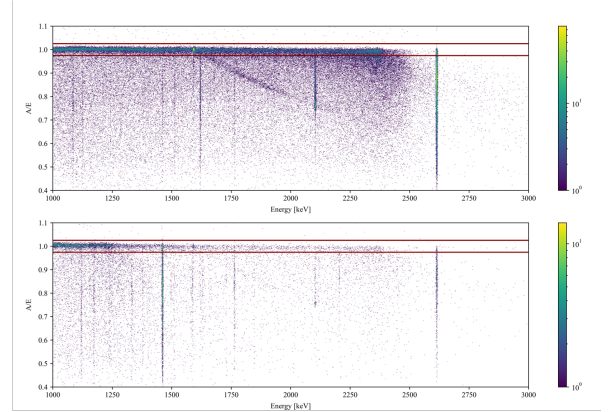


FIG. 9. A/E versus energy distributions of the ^{228}Th calibration data (top) and the 186.4 kg-day exposure data (down). The red lines indicate the A/E acceptance region for SSEs.

calibration data (top) and the 186.4 kg-day exposure data (down). The low A/E cut removes MSEs. Events rejected by the high A/E cut are likely to be γ events originating from the surface contamination and the p+ electrode.

Selected SSEs in the 186.4 kg-day exposure data are used to evaluate the energy resolution of $0\nu\beta\beta$ signals, indicated as the full width at half maximum (FWHM), as shown in Fig. 10. Gamma peaks from ^{208}Tl (583.3 keV, 1592.5 keV, 2614.5 keV), ^{214}Bi (609.3 keV), ^{228}Ac (911.2 keV) and ^{40}K (1460.8 keV) are used to calculate the FWHM at 2039 keV. The FWHMs of the six peaks are fitted with a function $\text{FWHM} = \sqrt{a + bE}$, and the interpolation of FWHM at 2039 keV is 2.85 keV. Uncertainties of the result mainly originate from two aspects:

- (1) Uncertainties from FWHMs of the selected characteristic gamma peaks and their effects on curve parameters (a, b): The uncertainties are calculated within the standard chi-square fitting and error propagation techniques. The combined uncertainty is ± 0.24 keV.
- (2) Choice of characteristic gamma peaks: Systematic

effects are taken as deviations of results due to the choice of gamma peaks. The FWHM curve is refitted without one of the six aforementioned peaks, and the maximum deviations in the FWHM at 2039 keV is 0.41 keV when the 2614 keV peak is excluded.

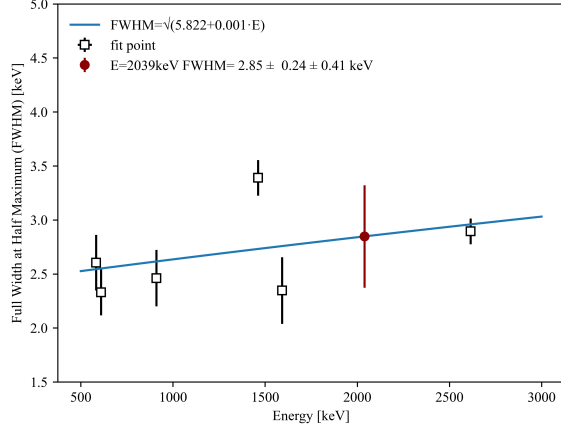


FIG. 10. Energy resolutions of single-site events.

Combining both uncertainties, the FWHM at 2039 keV is given as (2.85 ± 0.48) keV

C. Efficiency calibration

The total $0\nu\beta\beta$ signal efficiency consists of: (i) the efficiency of the data quality cut (ϵ_{QC}), (ii) the efficiency of the two electrons emitted from $0\nu\beta\beta$ decay deposits all energy in the active volume of the detector (ϵ_{fed}), and (iii) the efficiency of PSD (ϵ_{PSD}). The trigger rate during data taken is measured to be 0.005 Hz, the dead time is negligible and not considered in the efficiency.

The efficiency loss due to the noise cut is negligible as a physical event can be rejected by the noise cut only when it is overlapped with a burst of noise event. And the coincidences of those two events are negligible because of the low trigger rate. The efficiency of the data quality cut is calculated by recorded physical events, given as $(94.37 \pm 0.49)\%$ where the error is the statistical uncertainty of the recorded events.

The n+ electrode on the side and top surface of the detector forms an inactive region, known as the dead layer, reducing the active volume of the detector. The dead layer of (1.18 ± 0.10) mm and (0.17 ± 0.10) mm for side and top surfaces have been measured in our previous work [32-34] and gives a $(91.1 \pm 0.96)\%$ active volume of the crystal.

The probability of $0\nu\beta\beta$ events deposit all energy in the active volume of the detector (ϵ_{fed}) is calculated by Monte Carlo simulations via a Geant4 based simulation

toolkit SAGE [35]. The $0\nu\beta\beta$ decays are uniformly sampled in the germanium crystal, events with full energy deposited in the active region are counted to calculate the efficiency. The efficiency (ϵ_{fed}) is $(86.71 \pm 0.84)\%$ where the error is derived from variations of the dead-layer thickness: efficiencies are calculated for the top dead-layer thickness ranging from 0.07~0.27mm and the side dead-layer thickness ranging from 1.08~1.28mm, the maximum deviation on results is counted as the uncertainty. The ϵ_{fed} is lower than the active volume because the two electrons in $0\nu\beta\beta$ decay may lose their energy in germanium by bremsstrahlung.

The ^{228}Th calibration data and pulse shape simulations (PSS) are used to determine the PSD efficiency. The PSS of the ^{228}Th calibration data is conducted within a pulse shape simulation module of the SAGE toolkit [36]. The A/E distributions derived from the PSS, the ^{228}Th calibration data and the 186.4 kg-day exposure data are compared in Fig. 11. Events from the DEP, the SEP, the full energy peak (FEP) and the Compton flat (1800~2200 keV) of ^{208}Tl 2614.5 keV γ lines are selected for comparison. Table. I lists the A/E cut removal and survival fractions of the simulation and the calibration data.

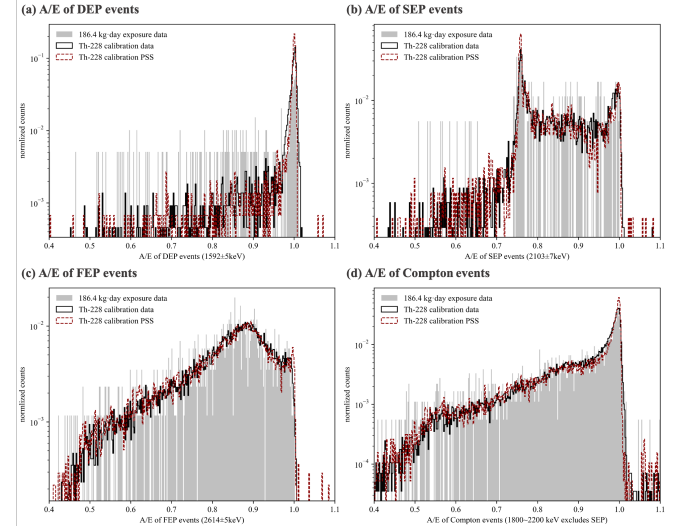


FIG. 11. A/E distributions derived from PSS, ^{228}Th calibration and 186.4 kg-day exposure data, for (a) the DEP events (1592 ± 5 keV), (b) the SEP events (2103 ± 7 keV), (c) the FEP events (2614 ± 5 keV), and (d) the Compton events (1800~2200 keV excludes SEP). All counts are normalized for comparison.

$0\nu\beta\beta$ events and DEP events are both typical SSEs but have different locations in the detector, $0\nu\beta\beta$ events are homogeneously distributed while DEP events are dominantly located at the corners. Therefore, the PSD efficiency of $0\nu\beta\beta$ events (ϵ_{PSD}) is calculated by a similar way of Gerda [37]: the removal fraction of the low A/E cut is adopted from the ^{228}Th calibration data as the low A/E cut only removes MSEs and $0\nu\beta\beta$ events and DEP

TABLE I. Removal fractions by the low A/E cut and high A/E cut and total survival fractions applying both cuts in ^{228}Th calibration data and pulse shape simulation data.

Region	Low A/E cut A/E < 0.975	High A/E cut A/E > 1.025	Survival fraction 0.975 < A/E < 1.025
^{228}Th calibration data			
DEP 1592.5 keV	6.76 \pm 0.67%	0.12 \pm 0.09%	93.12 \pm 3.32%
^{228}Th calibration PSS			
DEP 1592.5 keV	6.55%	1.43%	92.03%
$0\nu\beta\beta$ events PSS			
$Q_{\beta\beta}$ 2039 keV	6.99%	3.77%	89.23%

TABLE II. Uncertainties of $0\nu\beta\beta$ signal efficiency and their compositions, the combined efficiency and its uncertainty are listed in the last column.

Sources of Efficiency	Sources of Uncertainties	Value / [type]
Quality Cut $\varepsilon_{QC}=94.37\%$	Statistical uncertainty of recorded events	$\pm 0.49\%$ [stat]
$0\nu\beta\beta$ events full energy deposition $\varepsilon_{fed}=86.71\%$	Uncertainty on dead-layer thickness	$\pm 0.84\%$ [sys]
Pulse shape discrimination $\varepsilon_{PSD}=89.47\%$	Low A/E cut removal fraction of ^{228}Th calibration data	$\pm 0.67\%$ [stat]
	Variations on PSS parameters	$\pm 0.97\%$ [sys]
	Maximum discrepancy between experiment and PSS	$\pm 1.31\%$ [sys]
Combined efficiency	Efficiency = $\varepsilon_{QC} \cdot \varepsilon_{fed} \cdot \varepsilon_{PSD} = 73.21\%$ Uncertainty = $\pm 1.65\%$	

events are both typical SSEs. The removal fraction of the high A/E cut is adopted from the pulse shape simulation of $0\nu\beta\beta$ events. The calculation gives a PSD efficiency of 89.47%, similar to the result derived from the PSS (89.23%)

Statistical and systematic uncertainties of the PSD efficiency mainly consist of two parts:

- (1) The statistical uncertainty of the low A/E cut fraction of DEP events, $\pm 0.67\%$;
- (2) The systematic uncertainty of PSS: identical analyses are performed on varies PSS parameters, and the maximum deviation on results is adopted as one systematic uncertainty ($\pm 0.97\%$). The maximum deviation between the ^{228}Th calibration data and the PSS in Table. I ($\pm 1.31\%$) is added as the other systematic uncertainty. The combined systematic uncertainty is $\pm 1.63\%$.

Combining the statistical and systematic uncertainties, the ε_{PSD} is given as $(89.47 \pm 1.76)\%$.

Compositions of the $0\nu\beta\beta$ signal efficiency and their uncertainties are listed in Table. II. The total effi-

ciency is the product of the ε_{QC} , ε_{fed} , and ε_{PSD} , i.e. $(73.21 \pm 1.65)\%$.

D. Background model

Background spectra of different radioactive isotopes in different components of the detector setup are simulated using the SAGE toolkit. Table. III lists all the simulated background source and components. In our simulation, secular equilibrium is assumed in ^{238}U and ^{232}Th decay chain and all background sources are assumed to be uniformly distributed in their components. Due to the low muon flux in CJPL-I [25], backgrounds from muons and their secondary particles are negligible (less than 1×10^{-6} cpkkd). Neutrons are also negligible after shields of a 1 m polyethylene wall and a 20 cm borated polyethylene absorber. Therefore, they are not considered in the simulation. The $2\nu\beta\beta$ decays of ^{76}Ge are considered assuming a half-life of 2.1×10^{21} yr [38].

A background model (Fig. 12) is obtained by fitting the 186.4 kg-day spectrum with simulated spectra in 550~3000 keV energy range, using the maximum likeli-

TABLE III. Simulated background components and their contributions ($R_{0\nu\beta\beta}$) in the $0\nu\beta\beta$ signal region.

Sources	Components	$R_{0\nu\beta\beta}$
Cosmogenic isotopes	^{68}Ge , ^{60}Co , ^{54}Mn , ^{65}Zn in Ge	8.6%
	^{60}Co in Copper	2.1%
^{238}U chain	Crystal holder	15.1%
	Signal pin, Electronics	
	Vacuum Cup	
	Outer Shield	
^{232}Th chain	^{222}Rn	74.2%
	Crystal holder	
	Electronics	
	Vacuum Cup	
^{40}K	Outer Shield	0%
	Crystal holder	
	Electronics	
	Vacuum Cup	

hood method. The simulated spectra are convolved with an energy resolution function derived from fitting the FWHMs of the prominent gamma peaks in the spectrum prior to the PSD. Contributions of background sources in the $0\nu\beta\beta$ signal region are determined from the background model and are listed in Table. III.

In the $0\nu\beta\beta$ signal region ($Q_{\beta\beta} \pm 5\text{keV}$), 89% of the background are from radionuclides in the ^{232}Th and ^{238}U decay chains according to the background model. A background of 2.29×10^{-2} cpkcd in $Q_{\beta\beta} \pm 5\text{keV}$ region projected by the background model agrees well with $(2.13 \pm 0.3) \times 10^{-2}$ cpkcd calculated from the exposure data after unblinding.

IV. RESULTS AND DISCUSSION

Fig. 13 shows the measured energy spectra above 1000 keV for the 186.4 kg·day exposure data. Spectra shown in black and red are prior to and after the PSD, respectively. Spectra in the energy region of 1800~2300 keV are used to estimate the background in the $0\nu\beta\beta$ region of interest (ROI). Gamma peaks identified by the background model, as indicated by gray shading in the inset of Fig. 13, are excluded. Additionally, a $\pm 5\text{keV}$ wide window centered at $Q_{\beta\beta}$ is excluded, as indicated by the blue shaded region. Prior to and after PSD, the estimated background in the ROI from the resulting 420 keV window is $(2.45 \pm 0.06) \times 10^{-2}$ cpkcd and $(0.64 \pm 0.03) \times 10^{-2}$

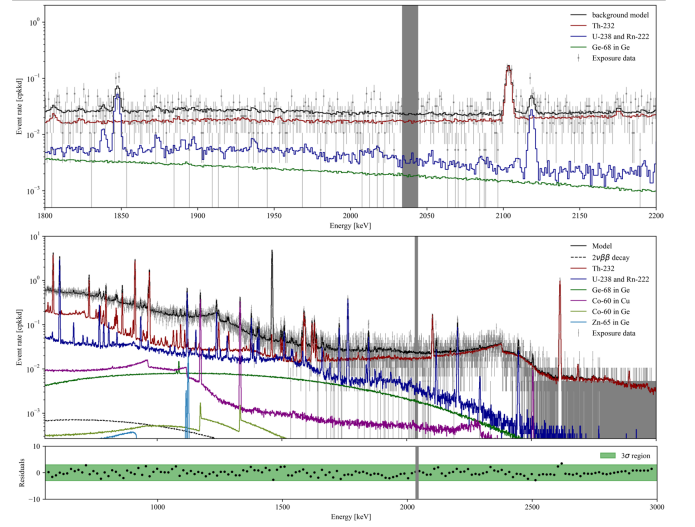


FIG. 12. Background model and its decompositions. Top panel shows spectra in 1800~2200 keV. Bottom panel shows spectra in 550~3000 keV. The simulated spectra are fitted with exposure data prior to the PSD, and the normalized residuals are shown under the spectra, the 3- σ band is marked in green. The blind regions ($Q_{\beta\beta} \pm 5\text{keV}$) are labeled in gray. The black dotted line is the expected $2\nu\beta\beta$ spectrum assuming a half-life of 2.1×10^{21} yr [38].

cpkcd, respectively. The background in the ROI is reduced by a factor of 3.79 after applying the PSD method.

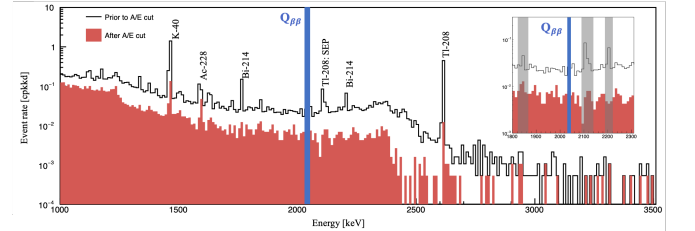


FIG. 13. Spectra of the 186.4 kg·day data, the main gamma lines are labeled in the spectrum prior to the PSD. The inset shows the same spectra in the background estimation window, which spans 1950~2350 keV, with regions excluded due to γ backgrounds shaded in gray and the 10 keV window centered at $Q_{\beta\beta}$ shaded in blue.

The exposure data after all cuts are used to analyze the $0\nu\beta\beta$ decay of ^{76}Ge . The half-life of ^{76}Ge neutrinoless double-beta decay can be calculated by Eq. 1:

$$T_{1/2}^{0\nu} = \frac{\ln 2 \cdot N_A \cdot f_{76} \cdot m \cdot T \cdot \varepsilon_{total}}{N^{0\nu} \cdot M} \quad (1)$$

Where $m \cdot T$ is the exposure, ε_{total} is the total efficiency defined in Sec III C, $N^{0\nu}$ is the number of observed $0\nu\beta\beta$ signal events, M the molar mass of natural Ge, N_A is the Avogadro's constant, f the fraction of ^{76}Ge atoms in the natural germanium detector.

Spectra of the 1940~2080keV analysis region are shown in Fig. 14. After unblinding, 178 events survive all data cuts, and eight events are found in the ROI ($Q_{\beta\beta} \pm 3\sigma_{\beta\beta}$).

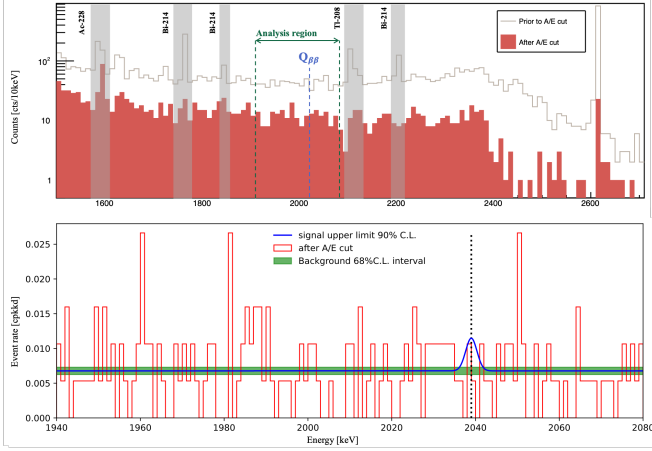


FIG. 14. Top panel: energy spectra of events before and after the A/E cut, green lines indicate the analysis region; Bottom panel: spectra of events survive all cuts in the analysis region, the blue line is the best fit background added with the 90%C.L. upper limit of the $0\nu\beta\beta$ signal strength, the green area is the 68%C.L. interval of the background fit result.

The $0\nu\beta\beta$ decay signal is analyzed using an unbinned extended profile likelihood method [39]. As predicted by the background model, no background peak is identified, and a flat background is assumed in the analysis region. The likelihood function is then given by:

$$f(E|b, N^{0\nu}) = \frac{1}{\Delta E \cdot b + N^{0\nu}} \times \left(b + \frac{N^{0\nu}}{\sqrt{2\pi} \cdot \sigma} e^{-\frac{(E - Q_{\beta\beta})^2}{2\sigma^2}} \right) \quad (2)$$

$$L(b, N^{0\nu}) = \frac{(\Delta E \cdot b + N^{0\nu})^N \cdot e^{-(\Delta E \cdot b + N^{0\nu})}}{N!} \times \prod_{i=1}^N f(E_i|b, N^{0\nu}) \quad (3)$$

Where N is the total events number in the analysis region, b is the background rate (cts/keV) and ΔE is the width of the analysis region, $N^{0\nu}$ the observed $0\nu\beta\beta$ events, E the energy of recorded events, σ is the energy resolution at $Q_{\beta\beta}$. $f(E|b, N^{0\nu})$ is the probability density function (pdf) of one single event. The likelihood function $L(b, N^{0\nu})$ is the product of the pdf of each event and extended with the Poisson term.

When fitting the likelihood function L , parameter b and $N^{0\nu}$ are bound to positive values. And a test statistic based on profile likelihood is used to calculate the confidence interval. The probability distributions of the test statistic are computed using the Monte Carlo method.

The unbinned profile likelihood analysis yields a best-fit background of 1.27 cts/keV and no indication for signal. The lower limit for $0\nu\beta\beta$ decay half-life is set to:

$$T_{1/2}^{0\nu} \geq 5.62 \times 10^{22} \text{ yr at 90\%C.L.} \quad (4)$$

The corresponding 90%C.L. upper limit of the $0\nu\beta\beta$ signal strength is 2.99 events. Uncertainties of the energy calibration (2039 ± 0.7 keV) and the energy resolution (2.85 ± 0.48 keV) are considered by folding them into the profile likelihood function through additional nuisance parameters constrained by Gaussian probability distributions. Uncertainties of the efficiency and the exposure are considered by propagating them through Eq. 1. The overall effect of all uncertainties on the half-life limit is about 2.42%.

The upper limit on the effective Majorana neutrino mass $m_{\beta\beta}$ is derived by:

$$(T_{1/2}^{0\nu})^{-1} = G^{0\nu} |g_A^2 \cdot M_{0\nu}|^2 \left(\frac{m_{\beta\beta}}{m_e} \right)^2 \quad (5)$$

$$m_{\beta\beta} \leq [4.6, 10.3] \text{ eV} \quad (6)$$

The upper and lower values are obtained by using nuclear matrix elements $M_{0\nu}$ from [40] and [41], respectively, the coupling constant g_A is set at 1.27 [12], and the phase factor $G^{0\nu}$ is adopted from [42], m_e is the electron mass.

As shown in Table. IV, compared with our previous $0\nu\beta\beta$ result from a p-type point contact germanium (PPCGe) detector in the CDEX-1 experiment [23], this work achieves a lower background by applying the PSD method. The CDEX-1 detector has a lower efficiency mainly due to the pulsed-reset preamplifier. The reset preamplifier is designed to have low electronic noise for dark matter detection and has a lower efficiency at the $Q_{\beta\beta}$ energy than the RC preamplifier used in this work.

As shown in Fig. 15, several key aspects to improve the $0\nu\beta\beta$ decay half-life sensitivity to meet the 10^{27} yr goal of the next-generation CDEX-300 ^{76}Ge $0\nu\beta\beta$ experiment are addressed:

a. increasing the effective exposure: enriching ^{76}Ge to 86% fraction and extending the single crystal to a 225 kg detector array, the sensitivity can be improved by at least 2 orders;

b. suppressing backgrounds in the $0\nu\beta\beta$ signal region: the current backgrounds in the $0\nu\beta\beta$ signal region are mainly from natural radioactivities of ambient materials, which can be reduced by a factor of 4 via the PSD method. Further reductions could be achieved by reducing the masses of surrounding materials, selecting ultra-pure materials, controlling cosmogenic isotopes in crystals via cooling or underground Ge fabrications, and the active veto techniques of the detector array and the LAr. The experiment could reach 10^{27} yr sensitivity with 1 ton-year exposure and a 1×10^{-4} cpkky background in the $0\nu\beta\beta$ signal region.

TABLE IV. Neutrinoless double-beta decay results from this work and CDEX-1.

	BEGe in This work	PPCGe in CDEX-1
Exposure	186.4 kg·day	304 kg·day
Total Efficiency	73.21%	68.44%
Background level	8.95 ± 0.22 cpkky (before PSD) 2.35 ± 0.11 cpkky (After PSD)	4.38 cpkky (w/o. PSD)
half-life limit (90% C.L.)	5.6×10^{22} yr	6.4×10^{22} yr

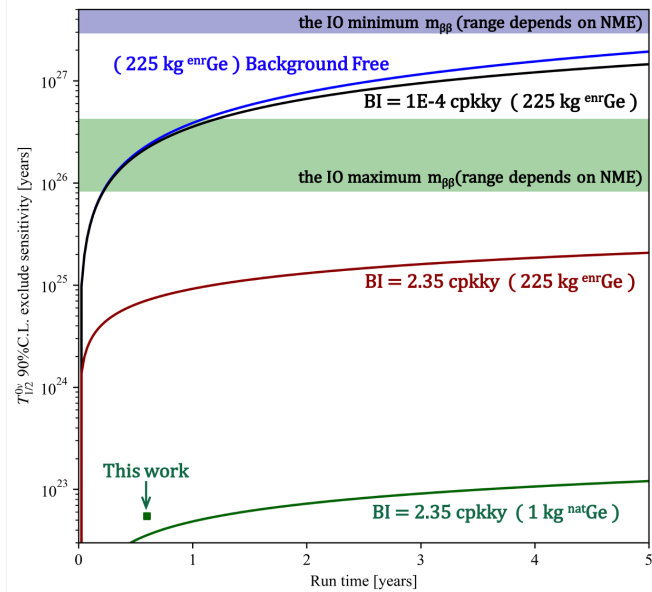


FIG. 15. The sensitivity of $0\nu\beta\beta$ decay half-life verses operating times for different background levels (BI) in the $0\nu\beta\beta$ signal region, ^{76}Ge enrichments and detector masses. The green and blue regions are the $0\nu\beta\beta$ decay half-life corresponding to the maximum and minimum effective neutrino mass $m_{\beta\beta}$, the range of which is dependent on the uncertainty of ^{76}Ge nuclear matrix element (2.66 6.04) [40-43]. The sensitivities are calculated using the approximation outline in [44] under the Poisson statistics, and the result of this work (the blue square) is calculated via an unbinned extended profile likelihood analysis.

V. SUMMARY

A prototype facility using a natural BEGe detector to search for $0\nu\beta\beta$ decay in ^{76}Ge is built in this work. Events selection and data analysis procedures are established to remove unphysical events, reconstruct energy, and discriminate background events. The pulse shape discrimination method (the A/E cut) is applied in data analysis and reduces the background in the $0\nu\beta\beta$ ROI by a factor of 3.79.

A background model is built for the prototype. Radionuclides from ^{232}Th and ^{238}U decay chains are identified as the primary source of backgrounds in the $0\nu\beta\beta$ signal region. Cosmogenic radioactive isotopes in germanium and copper also contribute to the backgrounds. To control backgrounds in the future large-scale experiment, (1) selecting ultra-pure materials can reduce the inhabit radioactive impurities from ^{232}Th and ^{238}U decay chains, (2) growing germanium crystal in an underground facility or cooling detector and copper material underground can reduce backgrounds from cosmogenic isotopes, (3) the anti-coincidence techniques can be used to further suppress backgrounds in the $0\nu\beta\beta$ signal region.

Based on the 186.4 kg·day exposure data, a limit on the half-life of ^{76}Ge $0\nu\beta\beta$ decay is set to 5.62×10^{22} yr at 90%C.L. via an unbinned extended profile likelihood method.

ACKNOWLEDGMENTS

This work was supported by the National Key Research and Development Program of China (Grant No. 2017YFA0402200) and the National Natural Science Foundation of China (Grants No. 12175112, No. 12005111, No. 11725522, No. 11675088, No.11475099).

- [1] Y. Fukuda, *et al.* (Super-Kamiokande), *Phys. Rev. Lett.* **81**, 1562 (1998).
- [2] Q. R. Ahmad, *et al.* (SNO Collaboration), *Phys. Rev. Lett.* **89**, 011301 (2002).
- [3] F. P. An, *et al.* *Phys. Rev. Lett.* **108**, 171803 (2012).
- [4] Y. F. Li, J. Cao, Y. Wang, and L. Zhan, *Phys. Rev. D*

- 88**, 013008 (2013).
- [5] Majorana and L. Maiani. *Il Nuovo Cimento.* **14**, 171 (1937).
- [6] J. D. Vergados, *et al.* *Rep. Prog. Phys.* **75**, 106301 (2012).
- [7] M. Bilenky, and C. Giunti. *Mod. Phys. Lett. A* **27**, 1230015 (2012).

- [8] S. Davidson, E. Nardi, and Y. Nir. Phys. Rept. **466**, 105 (2008).
- [9] A. Gando, *et al.* Phys. Rev. Lett. **110**, 062502 (2013).
- [10] Furry, W.H. Phys. Rev. **56**, 1184–1193 (1939).
- [11] M. Gunther, *et al.* (Heidelberg-Moscow), Phys. Rev. D **55**, 54 (1997).
- [12] M. Agostini, *et al.* (GERDA), Phys. Rev. Lett. **125**, 252502 (2020).
- [13] S. I. Alvis, *et al.* (Majorana), Phys. Rev. C **100**, 025501 (2019).
- [14] N. Abgrall, *et al.* (LEGEND), AIP Conf Proc. **1894**: 020027 (2017).
- [15] G. Anton, *et al.* (EXO-200), Phys. Rev. Lett. **123**, 161802 (2019).
- [16] A. Gando, *et al.* (KamLAND-Zen), Phys. Rev. Lett. **117**, 082503 (2016).
- [17] D. Adams, *et al.* (CUORE), Phys. Rev. Lett. **124**, 122501 (2020).
- [18] S. Andringa, *et al.* (SNO+), Adv. High Energy Phys. **2016**, 6194250 (2016).
- [19] R. Arnold, *et al.* (NEMO-3 experiment), Phys. Rev. D **92**, 072011 (2015).
- [20] E. Armengaud, *et al.* Eur. Phys. J. C. **80**, 44 (2020).
- [21] D.R. Artusa, *et al.* (CUPID), Phys. Rev. B **767**, 321-329 (2017).
- [22] D'Andrea. V, *et al.* Universe, **1**, 341 (2021).
- [23] L. Wang, *et al.* SCI CHINA PHYS MECH, **60**, 071011 (2017).
- [24] H. Ma, *et al.* J. Phys: Conf. Ser. **2156**, 012170 (2021).
- [25] Y. C. Wu, *et al.* Chin. Phys. C **37**, 086001 (2013).
- [26] Z. M. Zeng, *et al.* Nucl. Inst. Methods Phys. Res. Sect. A. **866**, 242-247 (2017).
- [27] V.T. Jordanov, *et al.* Nucl. Inst. Methods Phys. Res. Sect. A. **353**, 261–264 (1994).
- [28] M. Agostini, *et al.* (GERDA), Eur. Phys. J. C **75**, 255 (2015).
- [29] M. Agostini, *et al.* (GERDA), Eur. Phys. J. C **81**, 682 (2021).
- [30] M. Agostini, *et al.* Eur. Phys. J. C **73**, 2583 (2013).
- [31] D. Budjas, *et al.* J. Inst **4**, P10007 (2009).
- [32] Z. Zeng, *et al.* Nucl. Sci. Tech **28**, 71 (2017).
- [33] H. Jiang, *et al.* Chinese Phys. C **40**, 096001 (2016).
- [34] J. L. Ma, *et al.* Appl Radiat Isot. **127**, 130–136 (2017).
- [35] Z. She, *et al.* J. Inst. **16**, (2021).
- [36] W. Dai, in *Proceedings of the 13th National Conference on Particle Physics*, 2021.
- [37] M. Agostini, *et al.* (GERDA) Nature **544**, 47–52 (2017).
- [38] M. Agostini, *et al.* (GERDA) Eur. Phys. J. C **75**, 416 (2015).
- [39] G. Cowan, *et al.* Eur. Phys. J. C **71**, 1 (2011).
- [40] L. Coraggio, *et al.* Phys. Rev. C **101**, 044-315 (2020).
- [41] L. S. Song, *et al.* Phys. Rev. C **95**, 024-305 (2017).
- [42] J. Kotila and F. Iachello. Phys. Rev. C **85**, 034-316 (2012).
- [43] Abgrall N, *et al.* (LEGEND) arXiv **2107.11462**, (2021).
- [44] M. Agostini, *et al.* Phys. Rev. D **96**, 053001 (2017).